Acta Crystallographica Section A
Foundations of Crystallography
ISSN 0108-7673

Received 28 February 2002
Accepted 25 June 2002

Concerning intensity profiles observed in the 'real experiment'

Elisabeth Rossmanith

Mineralogisch-Petrographisches Institut der Universität Hamburg, Grindelallee 48, Germany. Correspondence e-mail: rossmanith@mineralogie.uni-hamburg.de

The modifications of the kinematical and extinction-corrected intensity profiles caused by the divergence of the incident synchrotron-radiation beam and the diffraction by the monochromator system are considered. Expressions for the integral width as well as the full width at half-maximum are presented and discussed. The theoretical results are compared with observations.

1. Introduction

In Ro-02,[1] the dynamical, kinematical and extinction-corrected intensity profiles of perfect crystals were considered. In the present paper, the modification of these profiles due to the experimental conditions of a measurement with synchrotron radiation will be analysed, directing attention on the width and shape of the intensity distributions of a perfect spherical crystal. In §2, expressions for the shapes, the integral width and the full width at half-maximum (FWHM) of the kinematical (§2.1) and extinction-corrected profiles (§2.2) are given. The modification of the profile shape caused by the characteristics of the synchrotron radiation at the beamline D3 at HASYLAB, DESY, considering the monochromator system in the framework of the kinematical theory, is discussed in §3. In §4, the corresponding results derived in the framework of the dynamical theory are presented. In §5, the theoretical intensity profiles are compared with profiles of a spherical perfect Si sample, measured with synchrotron radiation at six different wavelengths.

2. Intensity distribution functions for a perfect spherical crystal. Monochromatic parallel incident beam

2.1. The kinematical profile

Using the abbreviation $1/\Lambda = r_0\lambda|F|K/V_{\rm cell}$, where Λ is the extinction length, r_0 is the classical electron radius, λ is the wavelength of the radiation used for diffraction, F is the structure factor, $V_{\rm cell}$ is the volume of the unit cell, K is the polarization coefficient equal to 1 and $|\cos 2\theta|$ for the parallel and the perpendicular component of the X-ray electric field, respectively, and θ is the Bragg angle, the intensity $I^{\rm kin}_{\rm sphere}$ for a particular ω step of a perfect spherical crystal with radius r can be expressed as [Ro-02-(19)]

$$I^{\rm kin}_{\rm sphere} = (I_0 q)R^{\rm kin}_{\rm sphere} = (I_0 q)\tfrac{4}{3}(r/\Lambda^2)f(\zeta), \qquad (1)$$

where I_0 is the incident intensity, $q = 2r^2\pi$ is the cross section of the sphere and $R^{\rm kin}_{\rm sphere}$ is the kinematical reflectivity. The normalized intensity distribution function $f(\zeta)$ can be approximated by

$$\begin{aligned} f(\zeta) \cong (\Delta\zeta_{\rm integral})^{-1}[1 + 8(\pi r\zeta)^2 - \cos(4\pi r\zeta) \\ - 4\pi r\zeta \sin(4\pi r\zeta)]/[32(\pi r\zeta)^4], \end{aligned} \qquad (2)$$

where

$$\Delta\zeta_{\rm integral} = 2/(3r) \qquad (3)$$

is the integral width of the profiles (1) and (2). Expressing the distance of the particular reciprocal-lattice point from the Ewald sphere in the direction of the reflected beam, ζ, in terms of the rotation angle ω [see Ro-00*a*-(12)]

$$\zeta(\omega) = (1/\lambda^2 + |h|^2 - 2|h|\sin\omega/\lambda)^{1/2} - 1/\lambda, \qquad (4)$$

we obtain the ω-scan profile. In (4), $|h|$ is the length of the reciprocal-lattice vector $\mathbf{h}$ corresponding to the reciprocal-lattice point H. For intermediate Bragg angles, the integral width of the kinematical intensity profile, $\Delta\omega_{\rm integral}$, can be approximated by [Ro-00*a*-(16)]

$$\Delta\omega_{\rm integral} = \Delta\zeta_{\rm integral}\lambda/\sin 2\theta = 2\lambda/(3r\sin 2\theta), \qquad (5)$$

whereas the corresponding FWHM, $\Delta\omega_{\rm FWHM}$, calculated by means of *Mathematica* (Wolfram, 1999), is given by

$$\Delta\omega_{\rm FWHM} = 0.55333\lambda/(r\sin 2\theta). \qquad (6)$$

In Fig. 1, the normalized profile (2), represented as a function of ω (in degrees) for λ = 0.51 Å, r = 1 µm and θ = 5°, is compared with the Gaussian, I_G, as well as the Lorentzian distribution, I_L, having the same area (= 1) and the same integral width, $\Delta\omega_{\rm integral} = 0.0112°$:

$$\begin{aligned} I_G(\omega) &= \exp\{-\pi[\zeta(\omega)/\Delta\zeta_{\rm integral}]^2\}/\Delta\omega_{\rm integral} \\ I_L(\omega) &= 1/\{1 + [\pi\zeta(\omega)/\Delta\zeta_{\rm integral}]^2\}/\Delta\omega_{\rm integral}. \end{aligned} \qquad (7)$$

---

[1] Some of the expressions and figures discussed in this paper were derived or presented in previous papers of the author (Rossmanith, 1993*a*,*b*, 2000*a*,*b*, 2002). These expressions and figures will be referenced in the following by the abbreviation Ro-*xxy*-(*z*), where *xx* represents the two last digits of the year of publication, *y* stands for *a*, *b*, *c etc.* if more than one paper in the respective year is referenced and *z* represents the number of the expression or figure under consideration.

It is obvious from the figure that neither the Gaussian nor the Lorentzian distribution is an adequate approximation for the kinematical intensity profile. Furthermore, the form factor $\beta = \Delta\omega_{\rm FWHM}/\Delta\omega_{\rm integral} \cong 0.83$ of the kinematical intensity profile differs significantly from the form factors of the Gaussian, $\beta_G \cong 0.94$, as well as the Lorentzian distribution, $\beta_L \cong 0.64$ [see expressions (39) and (42) in Appendix *A*].

2.2. Extinction-corrected profiles

Extinction-corrected intensity profiles, $I^{\rm ext}_{\rm sphere}$, derived in the framework of the kinematical theory for spherical crystals are given by Becker & Coppens (1974), here referred to as B&C [see also Ro-02-(18)]. Unfortunately, a closed form of the reflectivity $R^{\rm ext}_{\rm sphere} = I^{\rm ext}_{\rm sphere}/(I_0 q)$ could be given by B&C only for 2θ = 0° (B&C.31) and 2θ = 180° (B&C.32):

$$\begin{aligned} R^{\rm ext}_{\rm sphere}(2\theta = 180^\circ) &= 1 - 4/(3R^{\rm kin}_{\rm sphere})\{1 - [\ln(1 + 3R^{\rm kin}_{\rm sphere}/2)] \\ &\quad \times (3R^{\rm kin}_{\rm sphere}/2)^{-1}\} \\ R^{\rm ext}_{\rm sphere}(2\theta = 0^\circ) &= \tfrac{1}{2} - 1/(3R^{\rm kin}_{\rm sphere})^2 + \exp(-3R^{\rm kin}_{\rm sphere})/(3R^{\rm kin}_{\rm sphere}) \\ &\quad + \exp(-3R^{\rm kin}_{\rm sphere})/(3R^{\rm kin}_{\rm sphere})^2. \end{aligned} \tag{8}$$

It will therefore be assumed in the following that for intermediate values of 2θ the profile can be calculated in a very first approximation according to

$$\begin{aligned} R^{\rm ext}_{\rm sphere}(\theta) &\cong \{R^{\rm ext}_{\rm sphere}(2\theta = 0^\circ)\}(90 - \theta)/90 \\ &\quad + \{R^{\rm ext}_{\rm sphere}(2\theta = 180^\circ)\}\theta/90. \end{aligned} \tag{9}$$

2.2.1. Intensity profiles obtained with the 'pull-down procedure'. The extinction-corrected profiles (8) are presented in Fig. 8 of Ro-02 for various $4r/3\Lambda = \bar{t}_{\rm in}/\Lambda$ ratios. The profiles are obtained by pulling down the 'reciprocal-lattice sphere' in the direction of the diffracted beam from outside to inside the Ewald sphere, *i.e.* the intensity is calculated as a function of ζ. It is obvious from this figure that for small $\bar{t}_{\rm in}/\Lambda$ ratios the two profiles are very similar and differ only marginally in their maximum values. With increasing $\bar{t}_{\rm in}/\Lambda$ ratio, the two profiles differ more and more. The maximum value of the reflectivity for back reflection (2θ = 180°) approaches the value 1, whereas for the forward reflection (2θ = 0°) the value 1/2 is obtained.

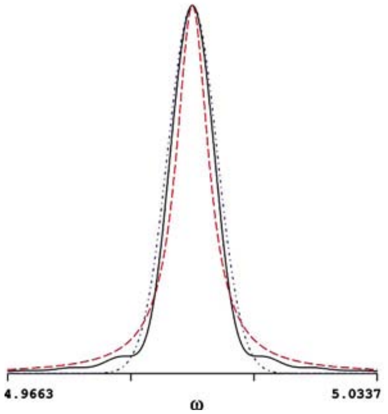

Figure 1
Black profile: the normalized intensity distribution function, equation (2), represented as a function of ω. λ = 0.51 Å, r = 1 μm and θ = 5°. Blue dashed (red chain-dotted) profile: the Gaussian distribution, I_G, (Lorentzian distribution, I_L) having the same area (= 1) and the same integral width as the black profile.

In Fig. 2(*a*), the black full lines show the integral widths *versus* the radius r of the sample, calculated according to

$$\Delta\zeta^{r/\Lambda}_{\rm integral} = \textstyle\int R^{\rm ext}_{\rm sphere}\,{\rm d}\zeta/R^{\rm ext}_{\rm sphere}(\zeta = 0) \tag{10}$$

with Λ = 1 (r and Λ in arbitrary units) for 2θ = 0° (upper curve) and 2θ = 180° (lower curve).

These widths are compared with the approximations (dashed red lines)

$$\begin{aligned} \Delta\zeta^{r/\Lambda}_{\rm integral}(2\theta = 180^\circ) &\approx [2/(3r)][1 + (1.03r/\Lambda)^2]^{1/2} \Rightarrow 0.7/\Lambda \\ \Delta\zeta^{r/\Lambda}_{\rm integral}(2\theta = 0^\circ) &\approx [2/(3r)][1 + (1.64r/\Lambda)^2]^{1/2} \Rightarrow 1.1/\Lambda, \end{aligned} \tag{11}$$

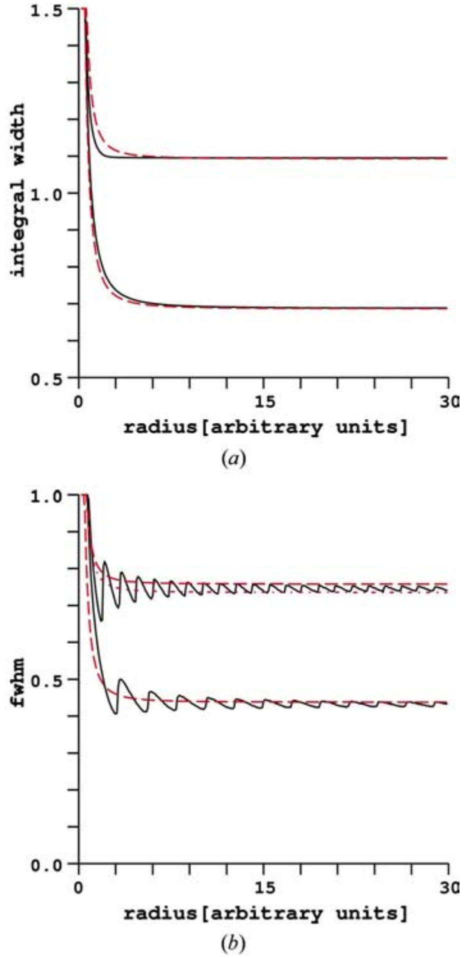

Figure 2
The widths of the profiles (8) for 2θ = 0° (upper curves) and 2θ = 180° (lower curves) *versus* the radius r of the sample, Λ = 1, r and Λ in arbitrary units. (*a*) $\Delta\zeta^{r/\Lambda}_{\rm integral}$: black full lines, expression (10); red dashed lines, approximations (11). (*b*) $\Delta\zeta^{r/\Lambda}_{\rm FWHM}$: black full lines, FWHMs of the profiles (8); red dashed lines, approximations (12); red chain-dotted line, the constant 1.03 in (12) is replaced by 1.

where the constants $c_1 = 1.64$ ($2\theta = 0°$) and $c_1 = 1.03$ ($2\theta = 180°$) were obtained by fitting the results of (11) to (10) for large r/Λ ratios. For small r/Λ ratios, both expressions (11) approach the kinematical integral width (3), whereas for large r/Λ ratios the integral width of the extinction-corrected profiles can be expressed as $\Delta\zeta^{r/\Lambda}_{\rm integral} = c_1[2/(3\Lambda)]$. For intermediate r/Λ ratios, however, the results of (11) deviate slightly from the results of (10).

The FWHMs of the profiles, $\Delta\zeta^{r/\Lambda}_{\rm FWHM}$, are presented as full black lines in Fig. 2(*b*). The saw-toothed appearance of the FWHMs *versus r* lines is easily explained by the oscillations of the corresponding intensity distributions [see Fig. 1, Fig. 3(*a*) and Ro-02-Fig. 8]. In Fig. 3, the extinction-corrected profiles (8) (black full lines) are compared with a Gaussian (blue dashed lines) and a Lorentzian distribution (red dashed lines), respectively, having the integral width defined by expression (11) for $2\theta = 180°$. It can be deduced from Fig. 3 that in the case of back reflection and increasing extinction the Lorentzian distribution becomes a fairly good approximation for the extinction-corrected intensity profile obtained with the 'pull-down procedure'. Bearing in mind that for a Lorentzian distribution the FWHM is related to the integral width by the form factor $2/\pi$ and that in the case $2\theta = 0°$ and large r/Λ ratios the maximum of the extinction-corrected profile is limited to the value $I(\zeta)^{\rm ext}_{\rm sphere}/(I_0 q) = 1/2$, it can be concluded that the width, $\Delta\zeta^{r/\Lambda}_{\rm FWHM}$, of this profile is about the width of the Lorentzian at $I_L(\zeta)/(I_0 q) = 1/4$. Therefore, it can easily be shown that for large r/Λ ratios

$$\begin{aligned}\Delta\zeta^{r/\Lambda}_{\rm FWHM}(2\theta = 180°) &\approx (2/\pi)[2/(3r)][1 + (1.03r/\Lambda)^2]^{1/2}\\ &\Rightarrow 0.44/\Lambda\\ \Delta\zeta^{r/\Lambda}_{\rm FWHM}(2\theta = 0°) &\approx (2/\pi)[2/(3r)][1 + 3(1.03r/\Lambda)^2]^{1/2}\\ &\Rightarrow 0.76/\Lambda \qquad (12)\end{aligned}$$

(red dashed lines in Fig. 2*b*). The red chain-dotted line in Fig. 2(*b*) is obtained by replacing in (12) the constant 1.03 by 1. It is obvious from the figure that, for $2\theta = 180°$ and large r/Λ ratios, the exact FWHM lies between these two approximations.

In Fig. 4, the black full lines represent the profiles for intermediate Bragg angles calculated according to expression (9) [Figs. 4(*a*), (*b*), (*c*): $\theta = 85, 45, 5°$, $r/\Lambda = 3$; Fig. 4(*d*): $\theta = 5°$,

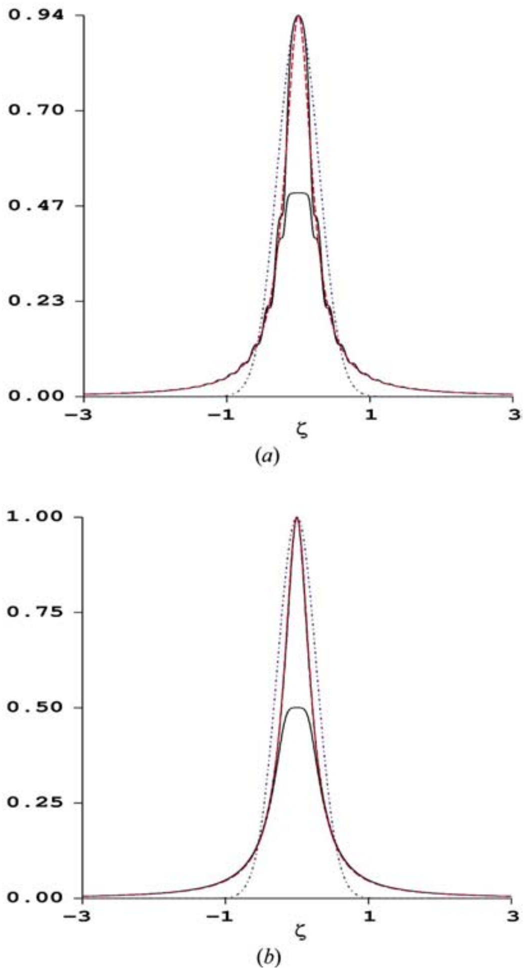

Figure 3
$R^{\rm ext}_{\rm sphere}$ *versus* ζ [(units of $r)^{-1}$]. Black full lines: the extinction-corrected profiles (8). Blue (red) dashed lines: the Gaussian (Lorentzian) distribution having the integral width defined by expression (11) for $2\theta = 180°$. (*a*) $r/\Lambda = 3$. (*b*) $r/\Lambda = 30$.

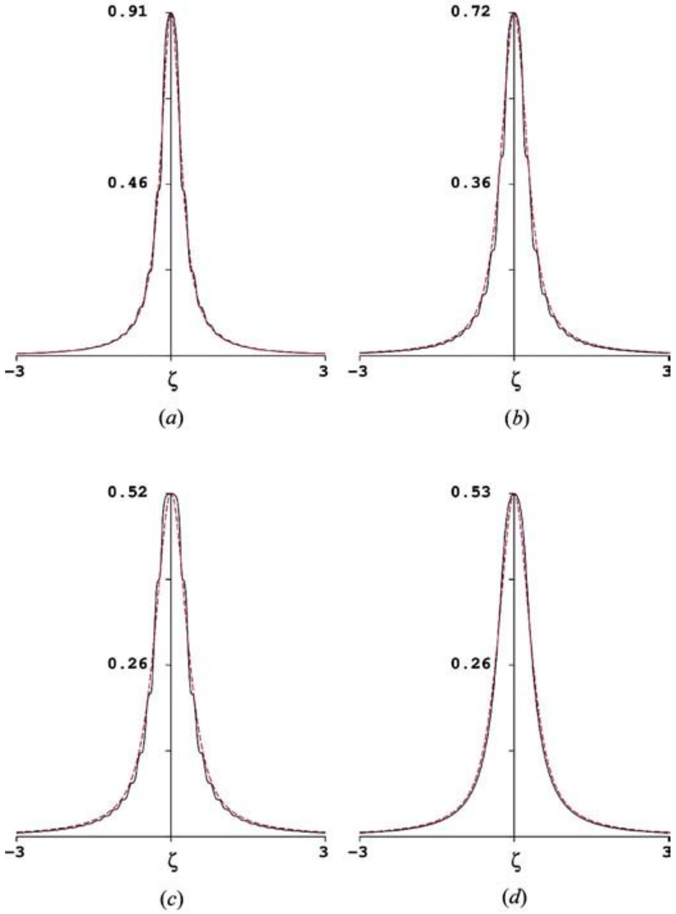

Figure 4
$R^{\rm ext}_{\rm sphere}$ *versus* ζ for intermediate Bragg angles. Black full profiles: calculated according to expression (9). Red dashed lines: pseudo-Voigt distributions defined by (13) with FWHMs calculated according to (14). (*a*) $\theta = 85°$, $r/\Lambda = 3$, $\eta = 0.95$. (*b*) $\theta = 45°$, $r/\Lambda = 3$, $\eta = 0.85$. (*c*) $\theta = 5°$, $r/\Lambda = 3$, $\eta = 0.80$. (*d*) $\theta = 5°$, $r/\Lambda = 30$, $\eta = 0.80$.

$r/\Lambda = 30$]. The red dashed lines in the figures are pseudo-Voigt distributions [see expression (44) in Appendix A], $R^{\rm PV}$, defined by

$$R^{\rm PV} = R^{\rm ext}_{\rm sphere}(\zeta = 0)[(1 - \eta)G_N + \eta L_N], \qquad (13)$$

where η is the mixing parameter giving the proportion of the Lorentzian contributions. The FWHM of these pseudo-Voigt distributions, which is equal to the FWHM of the contributing normalized Gaussian, G_N, and Lorentzian, L_N, is calculated according to

$$\Delta\zeta^{r/\Lambda}_{\rm FWHM}(\theta) \cong \{\Delta\zeta^{r/\Lambda}_{\rm FWHM}(2\theta = 0^\circ)\}(90 - \theta)/90 + \{\Delta\zeta^{r/\Lambda}_{\rm FWHM}(2\theta = 180^\circ)\}\theta/90. \qquad (14)$$

It is obvious from Figs. 4(*a*), (*b*) and (*c*) that the mixing parameter η depends on the Bragg angle [Figs. 4(*a*), (*b*), (*c*), (*d*): η = 0.95, 0.85, 0.80, 0.80] and that – even for $\theta = 5^\circ$ – the pseudo-Voigt function calculated according to (13) and (14) is a reasonable approximation for the profiles (9).

2.2.2. Intensity profiles obtained with the ω-scanning technique. It should once more be emphasized that the profiles defined for intermediate Bragg angles by (9) are only very first approximations proposed in this paper. However, using these approximations, it can easily be shown that for intermediate Bragg angles the extinction-corrected ω-scan profile is equivalent in shape to that obtained during the 'pull-down procedure'. The profiles differ only in their abscissae and the dimension of the corresponding variable. The equivalence is caused by the linearity of the relation between ω and ζ, represented as a blue dashed line in Fig. 5, *i.e.* in the range represented in Fig. 5(*a*), ζ decreases linearly from $+3 \times 10^{-4}$ to -3×10^{-4} [Å^{-1}] during the ω scan from outside to inside the Ewald sphere. The black full line in Fig. 5(*a*) corresponds to the profile (9), calculated with the ζ–ω relation defined by (4) for r/Λ = 30, Λ = 1 µm, λ = 0.51 Å, θ = 45° and η = 0.85. The red dashed line represents the pseudo-Voigt distribution (13) with the FWHM defined by

$$\Delta\omega^{r/\Lambda}_{\rm FWHM} = \Delta\zeta^{r/\Lambda}_{\rm FWHM}(\theta)\lambda/\sin 2\theta. \qquad (15)$$

From the very good fit between the profile (9) and the pseudo-Voigt distribution, it can be concluded that (15) is a reasonable approximation for the FWHM of the extinction-corrected ω-scan profiles.

On the other hand, it should be noted that it is impossible to observe the 'closed-form' profiles, expressions (8), given by B&C for 2θ = 0 and 2θ = 180° only, with the ω-scanning technique. Besides the fact that in both cases the reflected beam coincides with the incident beam, in the – unfeasible – case 2θ = 0°, the reciprocal-lattice point would coincide with the zero point of the reciprocal lattice, *i.e.* it would lie on the ω axis. Consequently, the reflected intensity would be constant during rotation (ζ will be zero for all ω). In the vicinity of 2θ = 180°, the relation between ω and ζ is no longer linear (blue dashed line in Fig. 5*b*). The ω-scan profile (black line) becomes asymmetric and deviates strongly from that obtained with the 'pull-down' procedure, which will be very similar to that given in Fig. 3(*b*) for 2θ = 180°.

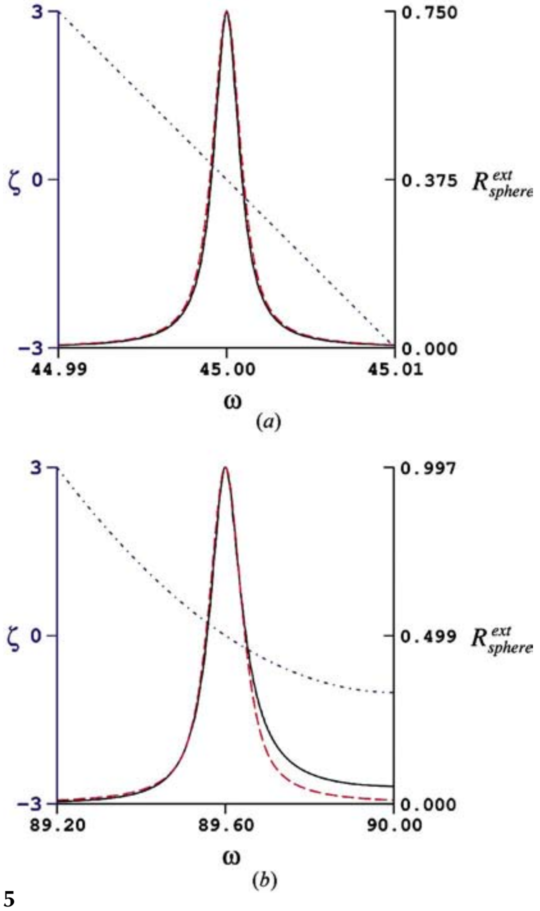

Figure 5
Intensity profiles obtained with the ω scanning technique. Blue dashed line: ζ [µm^{-1}] *versus* ω [°]. Black full line: profile (9) calculated with the ζ–ω relation defined by (4) for r/Λ = 30, Λ = 1 µm, λ = 0.51 Å. Red dashed line: pseudo-Voigt distribution (13) with the FWHM defined by (15). (*a*) θ = 45° and η = 0.85. (*b*) θ = 89.6° and η = 0.80.

3. Intensity distribution functions for a perfect spherical crystal. Kinematical diffraction by a triple-crystal system at a synchrotron-radiation source

In a '*real experiment*', the incident beam is neither exactly monochromatic nor exactly parallel. The wavelength spread and the divergence parallel and normal to the reflection plane of the primary reflection are caused by the X-ray source and the monochromator system as well as the diameter of the sample. The arrangement of the triple-crystal system used at the synchrotron-radiation source at beamline D3 at HASYLAB (DESY, Hamburg, Germany) was discussed in detail in Ro-93*a*. For simplicity, the monochromator system was considered in the framework of the kinematical theory, *i.e.* it was assumed that the reciprocal-lattice points corresponding to the 'very thick' perfect monochromator crystals (I and II in Fig. 6; see also Ro-93*a*-Figs. 1 and 2 and corresponding text) can be represented by dimensionless mathematical points. Consequently, kinematical diffraction is possible for ζ = 0 only, *i.e.* the reflecting planes of the two monochromator crystals both have to be exactly in Bragg position. It was shown in

Ro-93*a* that each ray diffracted by the planes of the two perfect monochromator crystals parallel to the reflection plane will have its characteristic wavelength, $\lambda^M_{\delta_p}$, depending on the angle δ^M_p between the particular ray and the central ray,

$$\lambda_{\delta^M_p} = 2d_M \sin(\theta_M + \delta^M_p), \tag{16}$$

where d_M is the interplanar spacing of the reflecting plane of the monochromator crystals and θ_M is the Bragg angle for the central ray. The measurements can be performed with the samples arranged antiparallel (position III*a* in Fig. 6) or parallel (position III*b*) with respect to the second monochromator crystal. Consequently, in the antiparallel arrangement, rays diffracted by the second monochromator crystal with negative δ^M_p and smaller wavelength ($\lambda_{\delta^M_p} < \lambda_{\delta^M_p=0}$) will correspond to a positive angle, δ^S_p, between the particular ray and the central ray at the sample and *vice versa*, *i.e.* $\delta^S_p = -\delta^M_p$. The opposite sign is obtained for the parallel arrangement. The corresponding wavelengths $\lambda + \delta_\lambda$ are therefore related to the δ^S_p according to

$$\lambda + \delta_\lambda = \lambda_{\delta^S_p} = 2d_M \sin(\theta_M \mp \delta^S_p) \tag{17}$$

with the minus (plus) sign corresponding to the antiparallel (parallel) arrangement.

Furthermore, it was shown in Ro-00*b*-Appendix *A*-(30) that, for a particular setting of the diffractometer angle ω and a particular incident ray with wavelength $\lambda_{\delta^S_p}$, divergences δ_n (normal) and δ^S_p (parallel to the reflection plane), ω-scan profiles of the sample in positions III*a*, III*b* in Fig. 6 can be calculated, replacing ζ given in (4) by

$$\begin{aligned}\zeta(\omega, \delta_n, \delta_p) = -1/\lambda_{\delta^S_p} + [1/\lambda^2_{\delta^S_p} + |h|^2 - 2|h| \cos \delta_n \\ \times \cos(90 - \omega - \delta^S_p)/\lambda_{\delta^S_p}]^{1/2},\end{aligned} \tag{18}$$

taking into account the probability $P(\delta_n, \delta^S_p)\,\mathrm{d}\delta_n\,\mathrm{d}\delta^S_p$ for this particular ray of the beam incident on the first monochromator crystal.

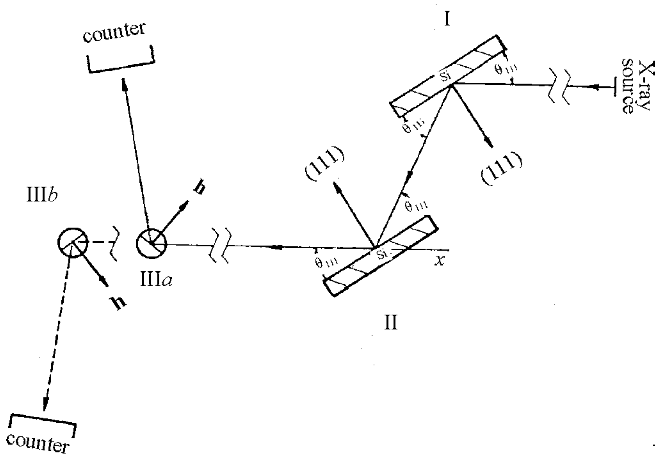

Figure 6
The arrangement of the triple-crystal system used at beamline D3 at the synchrotron-radiation source at HASYLAB.

For example, in the case of purely kinematical diffraction and $\delta_n = 0$, the total intensity recorded in the counter for a particular diffractometer angle ω has to be evaluated by

$$I(\omega) = \textstyle\int I^{\rm kin}_{\rm sphere}(\omega, \delta^S_p) P(\delta^S_p)\,\mathrm{d}\delta^S_p, \tag{19}$$

where $I^{\rm kin}_{\rm sphere}$ is defined by (1). According to Ro-93*a*-Fig. 3(*a*), the maximum divergence δ recorded by a spherical crystal bathed in the incident beam depends solely on geometrical factors and is independent of the wavelength

$$\delta = 2 \arctan[(s/2 + r)/L], \tag{20}$$

where s is the vertical dimension of the synchrotron-radiation source and L is the distance between the source and the sample (s = 0.11 cm and L = 3731 cm at beamline D3 at HASYLAB, $\delta = 0.00195^\circ$). Without the two monochromator crystals in the beam, in the case that the sample radius r is much smaller than s, the distribution function $P(\delta^S_p)$ will be nearly rectangular in shape, with constant probability for all the rays with $\delta^S_p \le \delta$ and zero probability for rays with $\delta^S_p > \delta$. In this section, *i.e.* in the framework of the kinematical theory, it will be assumed that the rectangular distribution function is smeared by the monochromator system, caused for example by imperfections in the crystals or by the fact that the corresponding reciprocal-lattice points are not exactly dimensionless mathematical points. The results represented in Fig. 7 are therefore obtained by replacing the rectangular distribution function by a Gaussian, P_G, in Fig. 7(*a*) and a Lorentzian distribution, P_L, in Fig. 7(*b*), having the area, the maximum value and the integral width of a rectangular distribution:

$$\begin{aligned}P_G(\delta^S_p) &= (1/\delta) \exp[-\pi(\delta^S_p/\delta)^2] \\ P_L(\delta^S_p) &= (1/\delta)[1 + (\pi\delta^S_p/\delta)^2]^{-1}.\end{aligned} \tag{21}$$

It should be noticed that (19) is not the convolution of the two distribution functions $I^{\rm kin}_{\rm sphere}$ and P. This can easily be demonstrated by replacing the normalized function f in (1) by the normalized distribution functions defined in (7). In Fig. 7(*a*), f is replaced by the Gaussian, I_G, in Fig. 7(*b*) by the Lorentzian distribution, I_L. For the sake of comparability of the width and shapes of the profiles, the intensities of all profiles in Fig. 7 are divided by the corresponding maximum value. It is obvious from the figures that the two black profiles obtained according to (19) for the two sample positions III*a* and III*b* (Fig. 6) differ appreciably in width for the Gaussian distributions $I^{\rm kin}_{\rm sphere}$ and P (Fig. 7*a*) as well as the Lorentian distributions (Fig. 7*b*). The same width, however, would be obtained for both positions in the case of a convolution, represented by the red dashed profiles. In the case of Fig. 7(*a*), the convolution results in a Gaussian and in the case of Fig. 7(*b*) in a Lorentzian distribution, with the FWHMs calculable according to

$$\begin{aligned}\Delta\omega_{{\rm FWHM},G} &= \beta_G\{[2/(3r)(\lambda/\sin 2\theta)]^2 + \delta^2\}^{1/2} \\ \Delta\omega_{{\rm FWHM},L} &= \beta_L[2/(3r)(\lambda/\sin 2\theta) + \delta].\end{aligned} \tag{22}$$

On the other hand, according to expression Ro-93*b*-(6b), which is based on purely geometrical considerations in reciprocal space, for a non-absorbing spherical crystal the FWHM consists of four terms, *i.e.* $\Delta\omega^{\delta}_{\rm FWHM}$, the broadening caused by the divergence, $\Delta\omega^{\Delta\lambda}_{\rm FWHM}$, the broadening caused by the wavelength spread, $\Delta\omega^{r/\Lambda}_{\rm FWHM}$, the broadening caused by the crystallite size and $\Delta\omega^{\eta}_{\rm FWHM}$, the broadening caused by the mosaicity of the crystal:

$$\begin{aligned}\Delta\omega^{\rm geom}_{\rm FWHM} &\cong \pm\Delta\omega^{\delta}_{\rm FWHM} + \Delta\omega^{\Delta\lambda}_{\rm FWHM} + \Delta\omega^{r/\Lambda}_{\rm FWHM} + \Delta\omega^{\eta}_{\rm FWHM}\\ &= \pm\beta^{\delta}\delta + \beta^{\delta}\delta\tan\theta/\tan\theta_M + \Delta\omega^{r/\Lambda}_{\rm FWHM} + \eta^{\rm mosaic}_{\rm FWHM},\end{aligned} \tag{23}$$

where β^{δ} is the form factor belonging to the distribution $P(\delta^S_p)$, and θ and θ_M are the Bragg angles of the sample and the monochromator, respectively. The plus signs in (23) correspond to the antiparallel (III*a*), the minus sign to the parallel sample position (III*b*) in Fig. 6. [It should be remembered that in the parallel arrangement expression (23) is valid only for sample reflections whose reciprocal-lattice vectors are equal to or greater than the lattice vector corresponding to the monochromator reflections, see Fig. 2(*b*) in Ro-93*b* and corresponding text.]

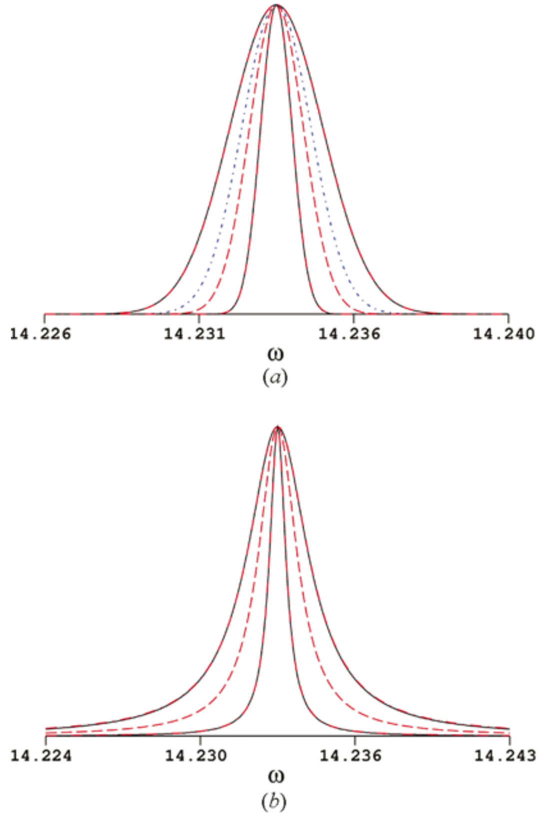

Figure 7
Discussion of the profile (19), calculated for the 111 reflection of Si, λ = 1.5418 Å, radius of the sample, r = 100 μm, $\delta = 0.00195°$. The intensities of all profiles are divided by their respective maximum values. Black lines: profile (19), obtained with $P(\delta^S_p)$, defined by the profile (21), and f replaced by the profile (7). Red dashed profiles: profiles with the FWHM, expression (22). Red chain-dotted profiles: profiles with the FWHM, expression (24) and (25), respectively. Blue dashed profile in (*a*): the Gaussian distribution with $\Delta\omega^G_{\rm FWHM} \cong \{[\delta\beta_G]^2 + [\delta\beta_G(\tan\theta/\tan\theta_M)]^2 + [2/(3r)(\lambda/\sin 2\theta)\beta_G]^2\}^{1/2}$. (*a*) $I^{\rm kin}_{\rm sphere}(\omega, \delta^S_p)$ and $P(\delta^S_p)$ replaced by Gaussians. (*b*) $I^{\rm kin}_{\rm sphere}(\omega, \delta^S_p)$ and $P(\delta^S_p)$ replaced by Lorentzians.

In the case of a perfect crystal, the mosaic spread $\eta^{\rm mosaic}_{\rm FWHM}$ is zero. The dashed-dotted red profiles in Fig. 7(*b*), which therefore correspond to Lorentzian distributions having the FWHMs calculated according to

$$\begin{aligned}\Delta\omega^L_{\rm FWHM} &\cong \beta_L\Delta\omega^L_{\rm integral}\\ &= \beta_L[\delta(\pm1 + \tan\theta/\tan\theta_M) + 2/(3r)(\lambda/\sin 2\theta)],\end{aligned} \tag{24}$$

coincide with the black full lines, indicating that, in the case when both distributions, $I^{\rm kin}_{\rm sphere}$ and P, are Lorentzian, expression (24) is an excellent approximation for the FWHMs of the two profiles obtained with (19).

In the case $I^{\rm kin}_{\rm sphere}$ and P are both Gaussian distributions (Fig. 7*a*), an excellent agreement between the black profiles and the dashed-dotted red Gaussian distributions are obtained with

$$\begin{aligned}\Delta\omega^G_{\rm FWHM} &\cong \beta_G\Delta\omega^G_{\rm integral}\\ &= \beta_G\{[\delta(\pm1 + \tan\theta/\tan\theta_M)]^2 + [2/(3r)(\lambda/\sin 2\theta)]^2\}^{1/2}.\end{aligned} \tag{25}$$

The blue dashed profile in Fig. 7(*a*), corresponding to a Gaussian distribution with

$$\begin{aligned}\Delta\omega^G_{\rm FWHM} \cong \{&[\delta\beta_G]^2 + [\delta\beta_G(\tan\theta/\tan\theta_M)]^2\\ &+ [2/(3r)(\lambda/\sin 2\theta)\beta_G]^2\}^{1/2},\end{aligned}$$

however, differs appreciably from the black lines, indicating that it is essential to add the terms $\Delta\omega^{\delta}_{\rm FWHM} = \pm\beta^{\delta}\delta$ and $\Delta\omega^{\Delta\lambda}_{\rm FWHM}$ linearly.

4. Dynamical diffraction by a double-monochromator system at a synchrotron-radiation source

The results of §3 are based on the assumption that the reciprocal-lattice point corresponding to a ’very thick’ monochromator crystal can be represented by a dimensionless mathematical point. It is obvious from §2.2, however, that, according to the kinematical extinction theory, even for large spherical crystals bathed in the incident beam, significant intensity of the reflected beam is observed in the ζ range of about $-2/\Lambda < \zeta < 2/\Lambda$. The same effect can be expected for a crystal of any shape, even for a plane parallel plate whose lateral extension is larger than the cross section of the incident beam, *i.e.* for the monochromator crystals. Consequently, the relation between the divergence and the wavelength will be more complicated than that given by expressions (16) and (17).

4.1. Dynamical diffraction profile for a thick plane parallel plate (symmetrical Bragg case). Monochromatic parallel incident beam

In this section, the discussion is restricted to centrosymmetric absorbing crystals with unlimited lateral extension, to situations where the Bragg planes are parallel to the crystal surface and the incident plane wave is polarized with its electric vector perpendicular to the reflection plane. For the symmetrical Bragg case, the monochromatic reflectivity $R_{\rm plate}$ for a thick plane parallel plate can be approximated by

Table 1
Real and imaginary parts of the structure factors of the Si 000 and Si 220 structure factors.

Extinction lengths and widths correspond to Figs. 8 and 10. See §4 for definitions.

λ (Å)	f'	f''	hkl	F'	F''	Λ (μm)	$\Delta\omega^D$, $\Delta\omega_{\rm centre}$ (″)	$\Delta\lambda^D$, $\Delta\lambda_{\rm centre}\times 10^6$ (Å)
1.5418	0.2547	0.3308	000	114.03	2.65	3.2	4.26	−73
			220	−69.17	−2.57	5.3	5.17	88
0.7709	0.0951	0.0841	000	112.75	0.67	6.5	1.05	− 9
			440	43.34	0.59	17.0	0.81	7
0.5139	0.0445	0.0363	000	112.35	0.29	9.8	0.47	−3
			660	−23.59	−0.22	46.9	0.20	1

[Zachariasen, 1945, expressions (3.116), (3.139), (3.179), (3.181), (3.189); Hirsch & Ramachandran, 1950, expressions (16), (19)]

$$\begin{aligned} R_{\rm plate} &= L - (L^2-1)^{1/2} \\ L &= \{y^2+g^2+|[(y^2-g^2-1+k^2)^2 \\ &\quad + 4(gy-k)^2]^{1/2}|\}/(1+k^2) \\ y &= -F'_0/|F'_h| - \pi\Lambda\zeta \\ g &= -F''_0|F'_h| \\ k &= F''_h/F'_h \\ \Delta\omega &= \omega-\theta = -\zeta\lambda/\sin 2\theta \end{aligned} \qquad (26)$$

In (26), $F_h = F'_h + iF''_h$ is the complex structure factor of index h and θ is the kinematical Bragg angle. In Fig. 8, the profiles of the fundamental Si 220 reflection (λ = 1.542 Å, red profile) and its next harmonics (440, $\lambda/2$, blue profile; 660, $\lambda/3$, green profile) are presented *versus* $\omega - \theta$. The anomalous-dispersion corrections for the atomic form factor, f' and f'' of Si (Table 1) were evaluated with the program *ABSORB* by Brennan & Cowan (1992). Fig. 8 is equivalent to Fig. 3.2 presented in Coppens (1992).

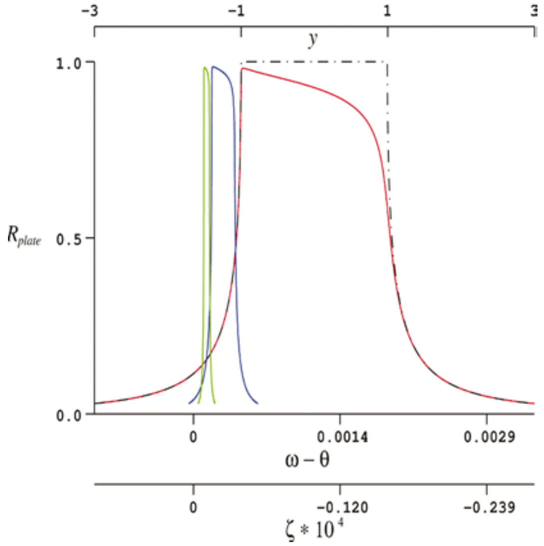

Figure 8
The profiles $R_{\rm plate}$. Red profile: the fundamental Si 220 reflection calculated for λ = 1.542 Å. Chain-dotted black profile: the fundamental Si 220 reflection calculated for λ = 1.542 Å and zero absorption ($g = k = f'' = 0$). Upper x axis: y scale. Middle x axis: $\Delta\omega = (\omega - \theta)$ scale [°]. Lowest x axis: ζ scale [Å^{-1}]. Blue profile: Si 440 reflection calculated for $\lambda/2$. Green profile: Si 660 reflection calculated for $\lambda/3$.

The Darwin width, given by Coppens (1992), expression (C-3.2),

$$\Delta\omega^D = (2/\pi)(1/\Lambda)(\lambda/\sin 2\theta) = \Delta\zeta^D(\lambda/\sin 2\theta), \qquad (27)$$

is equivalent to the angular range of total reflection of the single-crystal diffraction profile calculated for zero absorption [$g = k = f'' = 0$; chain-dotted black profile in Fig. 8; according to (26), for $-1 < y < 1$, $\Delta\zeta^D = 2/(\pi\Lambda)$ is obtained]. Since the area under the reflection curve of the profile (26) as well as its maximum depend on absorption, the same is true for the integral width as well as for the FWHM. On the other hand, in the case of zero absorption it is obvious from Fig. 8 that the FWHM is nearly equivalent to the Darwin width. Using expression (26), it can easily be shown by means of *Mathematica* (Wolfram, 1999) that for zero absorption

$$\begin{aligned} \Delta\omega^{f''=0}_{\rm integral} &= \tfrac{4}{3}\Delta\omega^D = \Delta\zeta^{f''=0}_{\rm integral}\lambda/\sin 2\theta \\ \Delta\omega^{f''=0}_{\rm FWHM} &= (3\times 2^{1/2}/2)\Delta\omega^D = \Delta\zeta^{f''=0}_{\rm FWHM}\lambda/\sin 2\theta. \end{aligned} \qquad (28)$$

It is interesting to compare these results for $\Delta\zeta^{f''=0}_{\rm integral} \cong 0.85/\Lambda$ and $\Delta\zeta^{f''=0}_{\rm FWHM} \cong 0.67/\Lambda$ with the widths (11) and (12) obtained for a spherical crystal with a large r/Λ ratio.

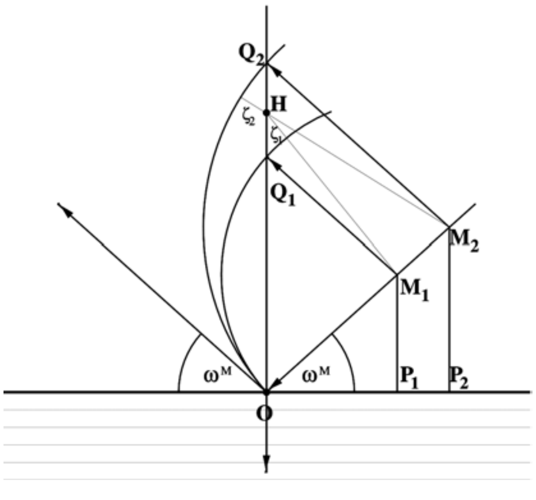

Figure 9
Dynamical diffraction in reciprocal space.

Caused by the first term of the variable y, in the Bragg case the value of the scan angle, $\omega_{\rm centre}$, corresponding to the centre of the diffraction pattern, $y = 0$,

$$\Delta\omega_{\rm centre} = \omega_{\rm centre} - \theta = [1/(\pi\Lambda_0)]\lambda/\sin 2\theta, \qquad (29)$$

is always greater than the Bragg angle. The corresponding $\zeta_{\rm centre} = -1/(\pi\Lambda_0)$ is negative, *i.e.* at the centre of the intensity profile the reciprocal-lattice point lies inside the Ewald sphere.

4.2. Wavelength range of the beam reflected by a thick plane parallel plate (symmetrical Bragg case). Parallel incident beam

The wavelength range of the beam reflected by the first monochromator crystal can easily be deduced from Fig. 9. The horizontal reflecting planes are parallel to the surface of the thick plane-parallel crystal plate with unlimited lateral extension. The reciprocal-lattice vector **h**, which is normal to the reflecting planes, connects the zero point of the reciprocal lattice O with the reciprocal-lattice point H. The vectors M_iO represent wave vectors corresponding to a ray with a particular angle of incidence, $\omega^M = \theta_M + \delta_p^M$. Each of the rays incident on the first monochromator crystal comprises the whole range of wavelengths of the continuous spectrum of the synchrotron-radiation beam. The Ewald spheres corresponding to the particular wavelengths $\lambda_i = 1/M_iO$ are represented by the arcs. $\omega^M = \theta_M + \delta_p^M$, the angle of incidence, is identical for the different wave vectors M_iO. According to (26), the diffracted intensity will depend on the particular wavelength λ_i and the corresponding ζ_i. Considering the triangles OM_iH ($M_iH = 1/\lambda_i + \zeta_i$, $M_iO = 1/\lambda_i$, $OH = |h|$), the relation $\lambda_i = 2(|h|\sin\omega^M + \zeta_i)/(|h|^2 - \zeta_i^2)$ can easily be obtained. The wavelength range $\Delta\lambda = \lambda_2 - \lambda_1$ corresponding to the range of total reflection, $-1 < y < 1$,

$$\Delta\lambda^D = 4d_M^2/(\pi\Lambda_h) = \lambda(\Delta\omega^D/\tan\theta_M), \qquad (30)$$

is obtained, bearing in mind that $\zeta_i^2 \ll |h|^2$ and inserting for $\zeta_1 = -1/(\pi\Lambda_h) - 1/(\pi\Lambda_0)$ and $\zeta_2 = +1/(\pi\Lambda_h) - 1/(\pi\Lambda_0)$. This result is identical with Coppens's (1992) expression (3.4). The centre of the wavelength range, $\lambda^{\rm centre}_{\delta_p^M}$, corresponding to $y = 0$, is displaced from the wavelength, $\lambda_{\delta_p^M}$, defined in (16) by

$$\Delta\lambda_{\rm centre} = \lambda^{\rm centre}_{\delta_p^M} - \lambda_{\delta_p^M} = -2d_M^2/(\pi\Lambda_0). \qquad (31)$$

In Fig. 10, a surface plot of the reflectivity, $R_{\rm plate}(\delta_p^M, \lambda)$, for $-0.002 \le \delta_p^M \le 0.002°$ and $1.5414 \le \lambda \le 1.5420$ Å is shown for the Si 220 reflection. The corresponding values for $\Delta\lambda^D$

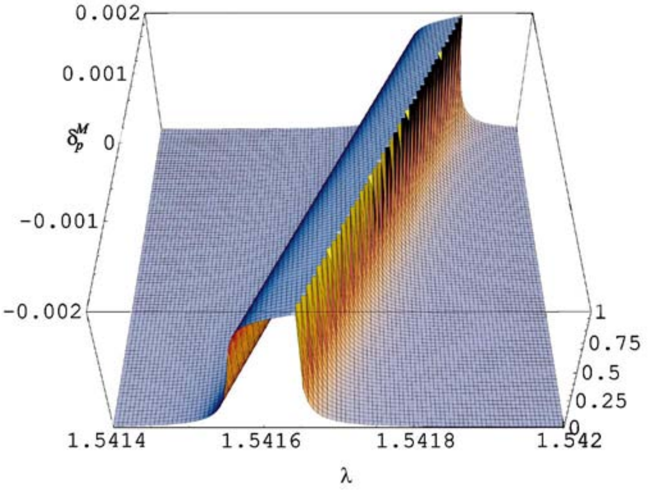

Figure 10
The surface plot of the reflectivity, $R_{\rm plate}(\delta_p^M, \lambda)$, calculated for the Si 220 reflection by means of *Mathematica*. x axis: $1.5414 \le \lambda \le 1.5420$ Å; y axis: $-0.002 \le \delta_p^M \le 0.002°$; z axis: $R_{\rm plate}(\delta_p^M, \lambda)$.

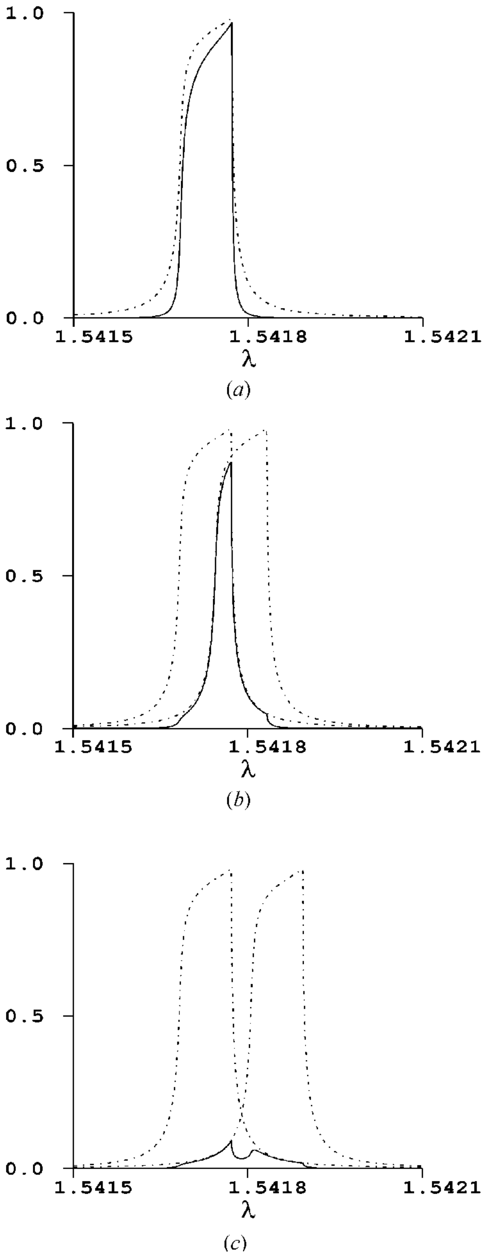

(*a*)

(*b*)

(*c*)

Figure 11
The wavelength distribution of the doubly diffracted ray. Full line: $P(\delta_p^M, \lambda)$ defined in equation (32). Dashed lines: the reflectivities for single diffraction, $R_{\rm plate}(\delta_p^M, \lambda)$, for Si 220. (*a*) Zero offset. (*b*) *c*2–*c*1 = 0.001°. (*c*) *c*2–*c*1 = 0.002°.

and $\Delta\lambda_{\rm centre}$ are given in Table 1. It is obvious from the figure that for each particular angle δ_p^M the wavelength $\lambda_{\delta_p^M}$ defined by (16) is now replaced by a wavelength distribution $R_{\rm plate}(\delta_p^M,\lambda)$. The centre of the corresponding profile, $\lambda_{\delta_p^M}^{\rm centre}$, is displaced from $\lambda_{\delta_p^M}$ by the constant term (31). The width of the wavelength range (30), on the other hand, is constant for all δ_p^M.

Considering the diffraction by the second monochromator crystal, it is essential to know the exact direction of the rays diffracted by the first monochromator. The direction of these rays can be deduced from Fig. 9. According to the dynamical theory (Section 28*c* in von Laue, 1960), the tangential components OP_i of the external (vacuum) and internal (crystal) wave vectors must be equal, *i.e.* for a particular index i, the points O, H and Q_i are lying on a common normal to the crystal surface. The points Q_i are therefore determined by this normal and the radius of the corresponding Ewald sphere, $1/\lambda_i$. In the symmetrical Bragg case, therefore, the angles at O and Q_i in the triangle OM_iQ_i are equal, *i.e.* for a particular divergence δ_p^M, for all wavelengths composing this ray, the angle of reflection is equal to the angle of incidence, $\omega^M=\theta_M+\delta_p^M$. As a consequence, as long as the second monochromator is exactly parallel to the first one, all rays reflected by the first monochromator crystal will meet the diffraction condition of the second monochromator. The wavelength distribution of the doubly diffracted ray (full line in Fig. 11*a*) is determined by the product of the reflectivities for single diffraction (dashed lines in Fig. 11). It is obvious from the figure that the FWHM of the full line in Fig. 11(*a*) is about the same as that of the chain dotted line. The two profiles, however, differ appreciably in shape and in their integral widths.

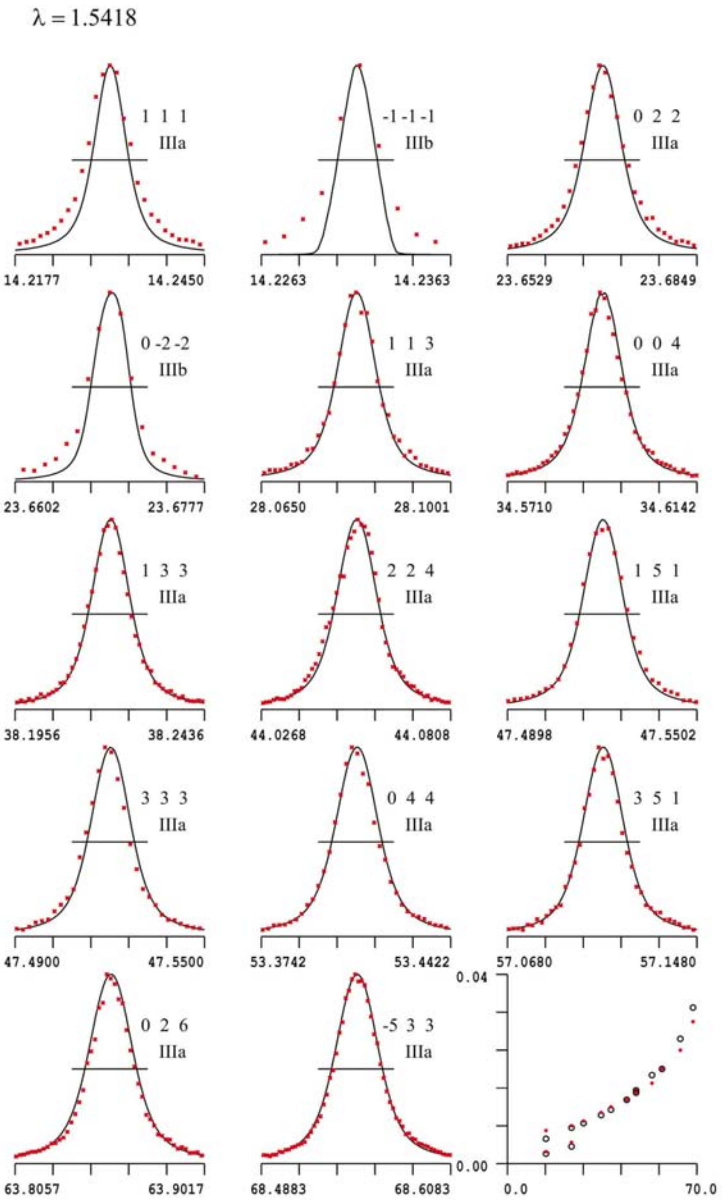

Figure 12
15 observed and theoretical intensity distributions. Red crosses: measured with synchrotron radiation at λ = 1.5418 Å. Black profiles: estimated according to expression (33) for the perfect spherical Si sample with radius r = 84 µm with zero offset. The Bragg reflections are marked by the indices *hkl* and the experimental position III*a* or III*b* defined in Fig. 6. Last diagram: the 15 experimental (red full circles) and theoretical (black circles) FWHMs [°] *versus* the Bragg angle [°].

To avoid higher-order contamination of the monochromated beam, a small offset from parallelism can be used to take advantage of the different wavelength ranges, $\Delta\lambda^D$, and the different displacements, $\Delta\lambda_{\rm centre}$, of the higher-order reflections. The effect on the fundamental Si 220 reflection is shown in Figs. 11(*b*) and 11(*c*). The full line represents the wavelength distribution of the doubly reflected beam

$$P(\delta_p^M,\lambda)=R_{\rm plate}(\delta_p^{M_1}=c1,\lambda)R_{\rm plate}(\delta_p^{M_2}=c2,\lambda) \quad (32)$$

for offsets $c2-c1$ = 0.001° and $c2-c1$ = 0.002°, respectively. It should be noted that the wavelength corresponding to the maximum of the profile is shifted to larger values. It is clear from the figure that the shape as well as the width of the wavelength profile strongly depend on the fine tuning of the parallel orientation of the second monochromator crystal.

5. Intensity profile of a perfect spherical crystal at a synchrotron-radiation source. Comparison with experimental profiles

Taking into account the results of the dynamical theory, after triple diffraction by two monochromator crystals and a spherical sample, the 'exact' total intensity obtained for a particular diffractometer angle, ω, with a divergent synchrotron-radiation beam has to be evaluated by

$$I(\omega)=I_0q\int R_{\rm sphere}^{\rm ext}(\omega,\delta_p^S)P(\delta_p^S)P(\delta_p^M,\lambda)\,{\rm d}\lambda\,{\rm d}\delta_p^S, \quad (33)$$

where $R_{\rm sphere}^{\rm ext}(\omega,\delta_p^S)$ and $P(\delta_p^M,\lambda)$ are defined by expressions (9) and (32). It should be noted that, firstly, the three profiles involved in (33) are different in shape and, secondly, they are neither Gaussian nor Lorentzian. Furthermore, as discussed in §3, the probability distribution $P(\delta_p^S)$ for the particular rays of the beam involved in the triple diffraction process is not known at all.

On the other hand, if all constituents were Lorentzian in shape, the FWHM of the profile obtained with (33) could be expressed as

$$\Delta\omega^L_{\rm FWHM} \cong \beta_L[\delta(\pm1+\tan\theta/\tan\theta_M)+(\Delta\lambda^D/\lambda)\tan\theta + \Delta\omega^{r/\Lambda}_{\rm integral}] \qquad (34)$$

and if all distribution functions involved in (33) were Gaussian in shape, the FWHM of the Bragg reflection profile, $\Delta\omega^G_{\rm FWHM}$, is given by

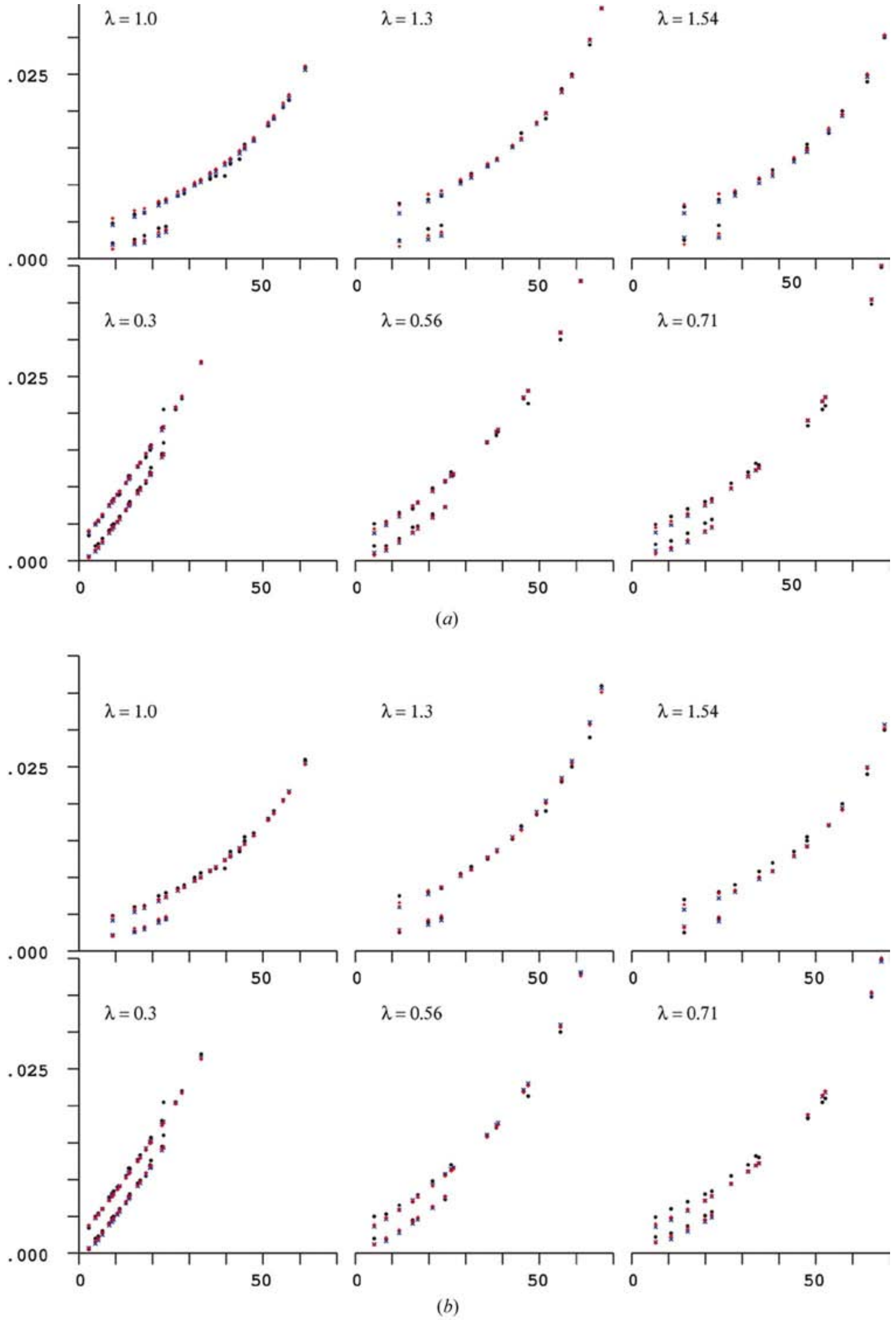

Figure 13
FWHMs [°] of a perfect spherical Si crystal with radius of 84 µm *versus* the Bragg angle [°] for six different wavelengths. Black full circles: experimental FWHMs. Red crosses: FWHMs corresponding to the 'Lorentzian' expression (34). Blue crosses: FWHMs corresponding to the 'Gaussian' expression (35). (*a*) Dynamical term neglected, *i.e.* $(\Delta\lambda^D/\lambda)\tan\theta = 0$. (*b*) Dynamical term taken into account, *i.e.* $(\Delta\lambda^D/\lambda)\tan\theta \neq 0$.

$$\Delta\omega^G_{\rm FWHM} \cong \beta_G\{[\delta(\pm 1 + \tan\theta/\tan\theta_M)]^2 + [(\Delta\lambda^D/\lambda)\tan\theta]^2 + [\Delta\omega^{r/\Lambda}_{\rm integral}]^2\}^{1/2}. \qquad (35)$$

In the following, the theoretical FWHMs will be compared with FWHMs of experimental profiles of an etched perfect spherical Si crystal with a radius of 84 µm. The measurements at six different wavelengths in the Bragg angle range $\theta < 70^\circ$ were performed at beamline D3 at HASYLAB, DESY[2] under the same conditions and in the same manner as described in Rossmanith *et al.* (1993). The 145 observed profiles are given as red crosses in Fig. 12 (14 profiles at λ = 1.5418 Å), only part of which is published here.[3] A first analysis of the data, based on the method introduced in Ro-93*a* and Ro-93*b*, *i.e.* based on (23), was performed by Schmidt (1995). In the present paper, the experimental FWHMs, given as black full circles in Fig. 13 and as red full circles in the corresponding diagrams of Fig. 12 and the deposit material, were re-determined fitting to the experimental data split-pseudo-Voigt distributions, defined by (47) and shown in Fig. 14(*b*). It was found that the observed X-ray synchrotron profiles can be well approximated by the symmetrical pseudo-Voigt (Fig. 14*a*) distribution, although (33) is not the convolution of Gaussian and Lorentzian functions. Consequently, an analysis of the Gaussian and Lorentzian components of the related Voigt functions (see Appendix *A*), which is very similar in shape to the pseudo-Voigt distribution, is senseless and will not be considered in the present paper. Attention will be restricted to the 'exact' expression (33).

However, as a first step it will be assumed that all distribution functions involved in (33) are either Lorentian or Gaussian in shape, *i.e.* in Fig. 13(*b*) (lower six diagrams), the experimental widths are compared with the FWHMs corresponding to (34) and (35), given as red and blue crosses, respectively. In Fig. 13(*a*) (upper six diagrams), according to the kinematical theory presented in §3, the dynamical term, $(\Delta\lambda^D/\lambda)\tan\theta$, is neglected. The only parameter that is unknown in the expressions for the profile width is the integral width corresponding to the divergence of the incident beam, δ. This parameter was estimated for each wavelength, fitting the theoretical FWHMs to the experimental ones. The corresponding values for the FWHM, $\delta^{\rm FWHM}_{\rm exp}$, obtained in this way, are given in Table 2. It is interesting to note that the purely kinematical approach results in very similar parameters $\delta^{\rm FWHM}_{\rm exp}$ for the Lorentzian and Gaussian distribution functions, whereas the Gaussian FWHMs are appreciably larger in the case corresponding to Fig. 13(*b*). Furthermore, it is clearly visible that $\delta^{\rm FWHM}_{\rm exp}$ varies with the wavelength. The physical significance of the different results obtained for $\delta^{\rm FWHM}_{\rm exp}$ can be seen from Fig. 15. The black rectangle, having the width δ defined in (20), represents the rectangular normalized distribution $P(\delta^S_p)$ of the beam divergence introduced in §3. The blue (red) profiles in the Fig. 15(*c*) show the normalized Gaussian and Lorentzian distribution functions defined in (21), whereas the normalized Gaussian (blue) and Lorentzian (red) distribution functions given in Figs. 15(*a*) and 15(*b*) show the $P(\delta^S_p)$ defined by widths given in Table 2, corresponding to Figs. 13(*a*) and 13(*b*), respectively. It is obvious from Figs. 15(*a*) and 15(*b*) that the maxima of the normalized Gaussians and Lorentzians are no longer equal to the height of the rectangle. Whereas the reduction of the number of photons in the maxima can readily be explained, for example, by wavelength-dependent air scattering of the photons of the incident beam, it is difficult to find physically sound reasons for the enhancement of the photons in the forward direction in the case of some of the Gaussians. However, although equations (34) and (35) are valid only in the case the experimental Bragg intensity profiles as well as the profiles involved in expression (33) are all Gaussian or all Lorentzian in shape, fairly good agreement between the experimental and theoretical FWHMs

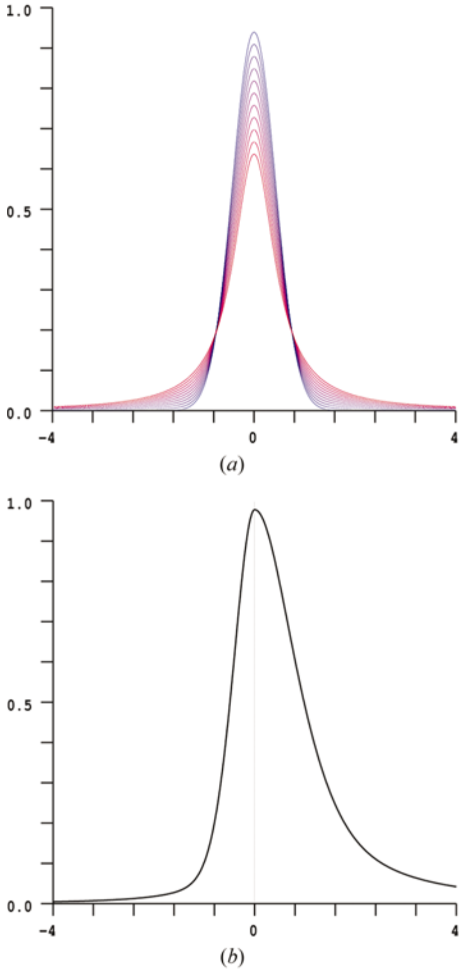

(*a*)

(*b*)

Figure 14
(*a*) The pseudo-Voigt function calculated for the mixing parameters η = 0.0 (blue, purely Gaussian), 0.1, 0.2, . . . , 0.9, 1.0 (red, purely Lorentzian), x scale in FWHM units. (*b*) The normalized split-pseudo-Voigt function $PV^{\rm split}_N$ calculated for $\Delta x_{\rm FWHM(x<0)} = 0.5$ and $\Delta x_{\rm FWHM(x>0)} = 1$, and mixing parameters, $\eta_{x<0} = 0.4$ and $\eta_{x>0} = 0.8$, x scale in $\Delta x_{\rm FWHM(x<0)}$ units.

---

[2] The measurement was performed in 1994. The author is indepted to K. Eichhorn, G. Kumpat, R. Kurtz and G. Ulrich for valuable support during the measurement.

[3] The rest of Fig. 12 has been deposited (19 profiles at λ = 1.3 Å; 29 profiles at λ = 1.0 Å; 19 profiles at λ = 0.7106 Å; 23 profiles at λ = 0.5607 Å; 41 profiles at λ = 0.3 Å) and is available from the IUCr electronic archives (Reference: MM0026). Services for accessing these data are described at the back of the journal.

Table 2
$\delta_{\rm exp}^{\rm FWHM}$ corresponding to Figs. 13, 15(*a*) and 15(*b*).

L: all distributions involved in equation (33) are Lorentzian in shape; *G*: all distributions involved in equation (33) are Gaussian in shape.

	$\delta_{\rm exp}^{\rm FWHM}(^\circ)\times 10^4$			
	$(\Delta\lambda^D/\lambda)\tan\theta = 0$ Fig. 13(*a*)		$(\Delta\lambda^D/\lambda)\tan\theta \neq 0$ Fig. 13(*b*)	
λ (Å)	*L*	*G*	*L*	*G*
0.3	18.5	18.3	15.9	17.8
0.5607	17.8	17.8	13.7	16.9
0.7106	17.8	17.8	12.7	16.0
1.0	21.0	20.7	13.4	17.8
1.3	28.0	28.2	19.7	26.3
1.5418	27.1	27.2	15.9	22.5

is obtained for both distributions, with and without taking into account the dynamical term $(\Delta\lambda^D/\lambda)\tan\theta$. It can therefore be concluded that the four expressions can be used for the evaluation of approximate FWHMs with comparable success.

In the second step of the present investigation, in Fig. 12 and in the deposit material, the observed profiles (red crosses) are compared with the profiles (black lines) obtained with expression (33). In each diagram, the Bragg reflection is marked by the indices *hkl* and the experimental position, III*a* or III*b* defined in Fig. 6. The step widths of the experimental scans, $\Delta\omega_{\rm step}$, given in Table 3, can also be deduced from the ω-scan width (limits of the *x* axis given in each diagram) and the number of steps. The last diagrams in Fig. 12 and in the deposit material show the FWHMs *versus* the Bragg angle for the particular wavelength. The theoretical (black) profiles in each diagram were calculated for the perfect spherical Si sample with radius r = 84 µm and the Si 111 double monochromator system, *i.e.* $R_{\rm sphere}^{\rm ext}(\omega,\delta_p^S)$ is defined by (9) and $P(\delta_p^M,\lambda)$ was estimated according to (32) for the parallel arrangement with zero offset, with F' and F'' given in Table 3. $P(\delta_p^S)$, the only unknown distribution function in (33), was fitted to the experimental data, *i.e.* for each particular wavelength one distinct pseudo-Voigt distribution, defined by the FWHM and the mixing parameter η given in Table 3, was used for the calculation of the theoretical profiles (33). It is obvious from Fig. 12 and the deposited material that, apart from small Bragg angles, the theoretical distributions obtained with this method are good estimates for the observed Bragg intensity reflections. In Fig. 15(*d*), the various pseudo-Voigt estimates obtained for $P(\delta_p^S)$ for the different wavelengths are compared with the rectangular distribution $P(\delta_p^S)$ discussed in §3. It should be noticed that the mixing parameter η is small for the smallest wavelength (see Table 3), *i.e.* the corresponding distribution $P(\delta_p^S)$ obtained by the fitting process is nearly Gaussian. For λ = 1.5418 Å, on the other hand, the pseudo-Voigt distribution is nearly Lorentzian. It is obvious from Fig. 15 that for all three models, the Gaussian and Lorentian as well as the 'exact' model, the integral widths of the distributions $P(\delta_p^S)$, obtained by the fitting process, differ from that defined by (20), being larger in most cases, all having, however, the same order of magnitude.

For small Bragg angles, the experimental profile shapes and widths differ appreciably from those obtained with the 'exact' expression (33). Especially for the 111 reflection, measured in the position III*b*, for all wavelengths the observed distribution functions are more Lorentzian in shape and have larger FWHMs than the calculated ones. (For λ = 0.3 Å, the width of the reflection is smaller than the step width of the measurement, the profile was not observable, see Fig. 12 deposit material.) For the 111 reflection, the Bragg angle of the monochromator crystals is equal to that of the sample. Consequently, for the position III*b*, the first terms in (34) and (35) are zero. The theoretical profile is determined by the distribution functions $R_{\rm sphere}^{\rm ext}(\omega,\delta_p^S)$ and $P(\delta_p^M,\lambda)$ only, *i.e.* it depends on the offset from parallelism of the two monochromator crystals. The profiles presented in Fig. 12 were calculated for zero offset, whereas the experiment was performed with a small but unknown offset angle (the intensity incident on the sample was reduced to about $\frac{1}{2}$). However, comparison of $\bar{1}\bar{1}\bar{1}$ profiles calculated for position III*b* for different offset angles (Fig. 16: red crosses: measured with synchrotron radiation at λ = 1.5418 Å; black profile: $c2-c1$ =

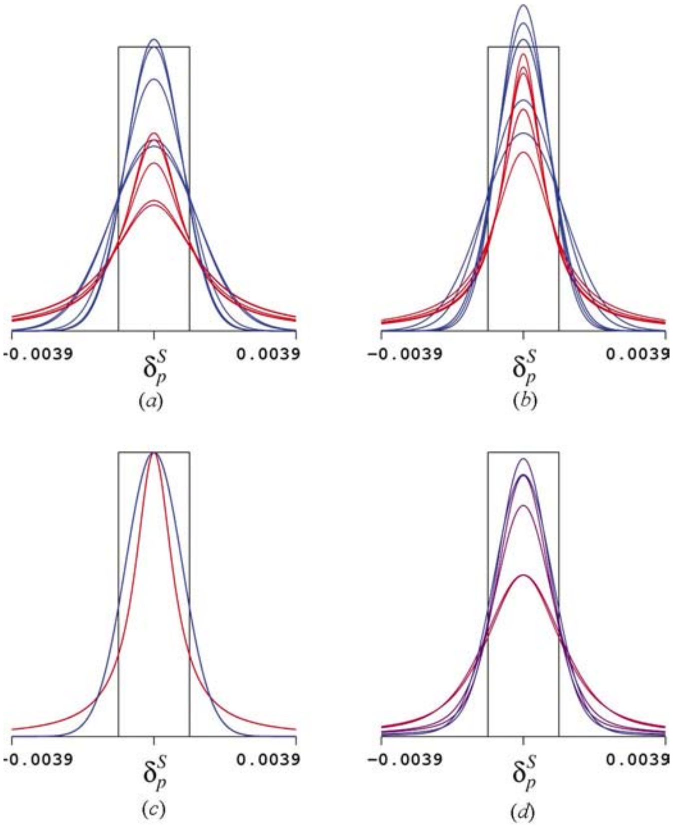

Figure 15
The probability distribution $P(\delta_p^S)$. In all diagrams, the black rectangular normalized distribution corresponds to the profile discussed in §3, *i.e.* the width $\delta = 0.00195^\circ$ of the rectangle is defined by expression (20). (*a*) and (*b*) Red (blue) profile: normalized Lorentzian (Gaussian) distributions corresponding to Figs. 13(*a*) and 13(*b*), respectively, with $\delta_{\rm exp}^{\rm FWHM}$ given for the various wavelengths in Table 2. (*c*) Red (blue) profile: normalized Lorentzian (Gaussian) defined in equation (21). (*d*) Normalized pseudo-Voigt distribution functions corresponding to Fig. 12 and deposit material, with $\delta_{\rm exp}^{\rm FWHM}$ and η given for the various wavelengths in Table 3.

Table 3
The real and imaginary parts of the Si 000 and Si 111 structure factors, $\delta^{\rm FWHM}_{\rm exp}$, and the mixing parameter η of the pseudo-Voigt distribution, $P(\delta^S_p)$, and the experimental step width, $\Delta\omega_{\rm step}$, corresponding to Fig. 12 and the deposit material.

Beamline D3 at HASYLAB/DESY, Si 111 double monochromator: a = 5.43 Å.

λ (Å)	F'_0	F''_0	F'_{111}	F''_{111}	$\delta^{\rm FWHM}_{\rm exp}$ (°) × 10^4	η	$\Delta\omega_{\rm step}$ (°) × 10^4
0.3	112.069	0.092	−58.094	−0.064	18.5	0.12	10
0.5607	112.418	0.349	−58.337	−0.244	17.2	0.26	10
0.7106	112.655	0.570	−58.503	−0.398	17.2	0.43	10–20
1.0	113.140	1.136	−58.842	−0.794	19.1	0.47	10–20
1.3	113.647	1.903	−59.196	−1.330	25.5	0.65	10–20–30
1.5418	114.030	2.646	−59.464	−1.850	24.2	0.78	10–20

0.0, equal with the corresponding profile in Fig. 12; green profile: $c2-c1$ = 0.001°; blue profile: $c2-c1$ = 0.002°) shows that the calculated intensity distribution – the shape as well as the width – is only marginally modified by the offset of 0.001°. Even in the case of the large offset angle, however, which would drastically reduce the intensity incident on the sample (see Fig. 11c), the theoretical profile does not fit the observed data, indicating that there is obviously an additional broadening effect which was neglected [δ_n = 0 in expressions (18) and (19)] or not considered (absorption, TDS *etc.*) during the derivation of (33). Broadening of the profiles can additionally be expected in the case of imperfections in the monochromator and/or sample crystals, which would modify the distributions $P(\delta^M_p, \lambda)$ and $R^{\rm ext}_{\rm sphere}(\omega, \delta^S_p)$. Last but not least, the kinematical approximations (8) and (9) for the profile shape of the intensity distribution $R^{\rm ext}_{\rm sphere}(\omega, \delta^S_p)$ may also be capable of improvement.

6. Conclusions

Expressions for the theoretical profiles observed in the '*real experiment*' were derived, considering the diffraction by the double monochromator system in the framework of the dynamical theory and the diffraction by the spherical perfect crystal sample in the framework of the kinematical extinction theory. It was shown that satisfactory agreement between theoretical and observed profile shapes can be obtained for reflections with intermediate and large Bragg angles, *i.e.* for intensity profiles whose width is dominated by the two wavelength-spread-dependent terms, $(\Delta\lambda^\delta/\lambda)\tan\theta$ and $(\Delta\lambda^D/\lambda)\tan\theta$. An exact evaluation of the profiles, however, is not possible, because at least the probability distribution, $P(\delta^S_p)$, of the divergent rays of the incident beam involved in the triple-crystal diffraction is not known. It turned out that distinct pseudo-Voigt distributions with wavelength-dependent FWHMs and mixing parameters were necessary to fit the experimental profiles. The profiles, $P(\delta^S_p)$, obtained with this fitting procedure are similar to those obtained in the two cases, when all the profiles involved in the diffraction process were either Lorentzian or Gaussian in shape. In addition, the agreement between the FWHMs of the 'exact' theoretical intensity profiles (33) and the experimental widths is comparable to that obtained with the approximations (34) and (35), replacing all profiles involved in the diffraction process by either Gaussians or Lorentzians, having the same area and the same integral width as the component distributions.

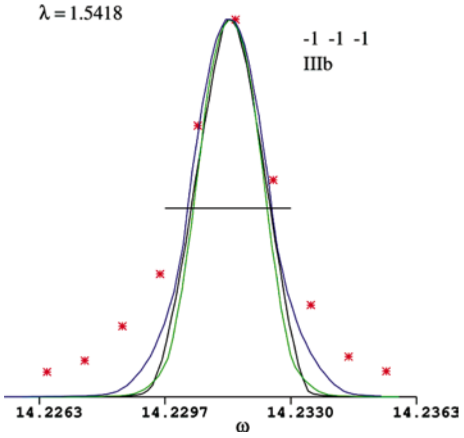

Figure 16
Observed and theoretical intensity distributions of the $\bar{1}\bar{1}\bar{1}$ reflection, position IIIb. Red crosses: measured with synchrotron radiation at λ = 1.5418 Å. Black (green, blue) profile: calculated according to expression (33) for the perfect spherical Si sample with radius r = 84 µm with zero offset (0.001°, 0.002° offset angle).

APPENDIX *A*
The Voigt and pseudo-Voigt functions

The following symbols will be used in the Appendix:

$\Delta x^i_{\rm integral}$ integral width of the distribution i

$\Delta x^i_{\rm FWHM}$ *FWHM* of the distribution i

$\beta_i = \Delta x^i_{\rm FWHM}/\Delta x^i_{\rm integral}$ form factor of the distribution i.

The convolution of two distribution functions f and g is defined by

$$h(x) = \int\limits_{-\infty}^{+\infty} f(x')g(x-x')\,{\rm d}x'. \tag{36}$$

(a) *If f and g are both normalized Gaussian distributions* G_N *defined by*

$$G_N = (1/\Delta x^G_{\rm integral})G \tag{37}$$

with

$$G = \exp[-\pi(x/\Delta x^G_{\rm integral})^2]$$

then h is also Gaussian with an integral width given by (Langford, 1978)

$$\Delta x^h_{\rm integral} = [(\Delta x^f_{\rm integral})^2 + (\Delta x^g_{\rm integral})^2]^{1/2}. \qquad (38)$$

The form factor of a Gaussian distribution results in

$$\beta_G = 2(\ln 2/\pi)^{1/2} = 0.93943. \qquad (39)$$

(*b*) *If f and g are both normalized Lorentzian distributions* L_N *defined by*

$$L_N = (1/\Delta x^L_{\rm integral})L \qquad (40)$$

with

$$L = [1 + (\pi x/\Delta x^L_{\rm integral})^2]^{-1},$$

then h is also Lorentzian with an integral width given by

$$\Delta x^h_{\rm integral} = \Delta x^f_{\rm integral} + \Delta x^g_{\rm integral}. \qquad (41)$$

The form factor of a Lorentzian distribution results in

$$\beta_L = 2/\pi = 0.63662. \qquad (42)$$

(*c*) *If f is Lorentzian and g is Gaussian then h is a Voigt distribution V* with an integral width given by

$$\Delta x^V_{\rm integral} = \Delta x^g_{\rm integral} \exp[-(1/\pi)(\Delta x^f_{\rm integral}/\Delta x^g_{\rm integral})^2] \times \left[1 - {\rm erf}\left(\frac{1}{\pi^{1/2}}\frac{\Delta x^f_{\rm integral}}{\Delta x^g_{\rm integral}}\right)\right]^{-1}. \qquad (43)$$

The Voigt function is very similar in shape to the normalized pseudo-Voigt function, PV_N, defined by (Parrish, 1992, expression 2.3.3.15)

$$\mathrm{PV}_N = (1-\eta)G_N + \eta L_N = [(1-\eta)\beta_G G + \eta\beta_L L]/\Delta x_{\rm FWHM}, \qquad (44)$$

where η is the mixing parameter giving the proportion of the Lorentzian contribution, $0 \le \eta \le 1$ and $\Delta x^{\rm PV}_{\rm FWHM} = \Delta x^G_{\rm FWHM} = \Delta x^L_{\rm FWHM} = \Delta x_{\rm FWHM}$. It can easily be shown that

$$\beta_{\rm PV} = (1-\eta)\beta_G + \eta\beta_L. \qquad (45)$$

Therefore it follows that

$$\Delta x^V_{\rm integral} \approx \Delta x^{\rm PV}_{\rm integral} = \Delta x^{\rm PV}_{\rm FWHM}/\beta_{\rm PV}, \qquad (46)$$

i.e. refined η and $\Delta x_{\rm FWHM}$ of a fitted experimental profile can be related by a polynomial expansion (Hastings *et al.*, 1984) to the widths of the Lorentzian and Gaussian components of the Voigt function. The pseudo-Voigt function, shown for different η in Fig. 14(*a*), is therefore frequently used to fit synchrotron-radiation profiles. Peak asymmetry can be incorporated by a normalized split-pseudo-Voigt function $\mathrm{PV}^{\rm split}_N$ (Fig. 14*b*) consisting of two halves, $\mathrm{PV}_{N,x<0}$ and $\mathrm{PV}_{N,x>0}$, with different widths, $\Delta x_{{\rm FWHM}(x<0)}$ and $\Delta x_{{\rm FWHM}(x>0)}$, and mixing parameters, $\eta_{x<0}$ and $\eta_{x>0}$, for the left and right side, respectively, but with a common maximum value $PV^{\rm split}_N(x=0)$:

$$\begin{aligned}\mathrm{PV}^{\rm split}_N(x<0) &= \{2\mathrm{PV}_{N,x>0}(x=0)/[\mathrm{PV}_{N,x<0}(x=0) \\ &\quad + \mathrm{PV}_{N,x>0}(x=0)]\}\mathrm{PV}_{N,x<0} \qquad (47)\\ \mathrm{PV}^{\rm split}_N(x>0) &= \{2\mathrm{PV}_{N,x<0}(x=0)/[\mathrm{PV}_{N,x<0}(x=0) \\ &\quad + \mathrm{PV}_{N,x>0}(x=0)]\}\mathrm{PV}_{N,x>0} \\ \mathrm{PV}^{\rm split}_N(x=0) &= 2\mathrm{PV}_{N,x>0}(x=0)\mathrm{PV}_{N,x<0}(x=0)/[\mathrm{PV}_{N,x<0}(x=0) \\ &\quad + \mathrm{PV}_{N,x>0}(x=0)].\end{aligned}$$

The FWHM and the integral width are obviously given by

$$\begin{aligned}\Delta x^{s-{\rm PV}}_{\rm FWHM} &= (\Delta x_{{\rm FWHM}(x<0)} + \Delta x_{{\rm FWHM}(x<0)})/2 \\ \Delta x^{s-{\rm PV}}_{\rm integral} &= 1/\mathrm{PV}^{\rm split}_N(x=0).\end{aligned} \qquad (48)$$

References

Becker, P. J. & Coppens, P. (1974). *Acta Cryst.* A**30**, 129–147.

Brennan, S. & Cowan, P. L. (1992). *Rev. Sci. Instrum.* **63**, 850-853.

Coppens, P. (1992). *Synchrotron Radiation Crystallography*. London/San Diego/New York/Boston/Sydney/Tokyo/Toronto: Academic Press.

Hastings, J. B., Thomlinson, W. & Cox, D. E. (1984). *J. Appl. Cryst.* **17**, 85–89.

Hirsch, P. B. & Ramachandran, G. N. (1950). *Acta Cryst.* **3**, 187–194.

Langford, J. I. (1978). *J. Appl. Cryst.* **11**, 10–14.

Laue, M. von (1960). *Röntgenstrahlinterferenzen*. Frankfurt am Main: Akademische Verlagsgesellschaft.

Parrish, W. (1992). *International Tables for Crystallography*, Vol. C, p. 67. Dordrecht: Kluwer Academic Publishers.

Rossmanith, E. (1993*a*). *Acta Cryst.* A**49**, 80–91.

Rossmanith, E. (1993*b*). *J. Appl. Cryst.* **26**, 753–755.

Rossmanith, E. (2000*a*). *J. Appl. Cryst.* **33**, 323–329.

Rossmanith, E. (2000*b*). *J. Appl. Cryst.* **33**, 1405–1414.

Rossmanith, E. (2002). *Acta Cryst.* A**58**, 12–20.

Rossmanith, E., Werner, M., Kumpat, G., Ulrich, G. & Eichhorn, K. (1993). *J. Appl. Cryst.* **26**, 756–762.

Schmidt, H. (1995). Diplomarbeit, Universität Hamburg, Germany.

Wolfram, S. (1999). *The Mathematica Book*, 4th ed. Wolfram Media/Cambridge University Press.

Zachariasen, W. H. (1945). *Theory of X-ray Diffraction in Crystals*. New York: John Wiley.